OPEN ACCESS
IOP Publishing | International Atomic Energy Agency Nuclear Fusion
Nucl. Fusion **63** (2023) 062001 (12pp) https://doi.org/10.1088/1741-4326/acc818

Probing non-linear MHD stability of the EDA H-mode in ASDEX Upgrade

A. Cathey[1,*], M. Hoelzl[1], L. Gil[2], M.G. Dunne[1], G.F. Harrer[3], G.T.A. Huijsmans[4,5], J. Kalis[1,6], K. Lackner[1], S.J.P. Pamela[7], E. Wolfrum[1], S. Günter[1], the JOREK Team[a], the ASDEX Upgrade Team[b] and the EUROfusion MST1 Team[c]

[1] Max Planck Institute for Plasma Physics, Boltzmannstr. 2, 85748 Garching, Germany
[2] Instituto de Plasmas e Fusão Nuclear, Instituto Superior Técnico, Universidade de Lisboa, 1049-001 Lisboa, Portugal
[3] Institute of Applied Physics, TU Wien, 1040 Vienna, Austria
[4] CEA, IRFM, 13108 Saint-Paul-Lez-Durance, France
[5] Eindhoven University of Technology, PO Box 513, 5600 MB Eindhoven, Netherlands
[6] Physik Department E28, Technische Universität München, Garching 85748, Germany
[7] CCFE, Culham Science Centre, Abingdon, Oxon OX14 3DB, United Kingdom of Great Britain and Northern Ireland

E-mail: andres.cathey@ipp.mpg.de

Received 9 December 2022, revised 22 March 2023
Accepted for publication 28 March 2023
Published 11 April 2023

Abstract

Regimes of operation in tokamaks that are devoid of large edge localised modes have to be better understood to extrapolate their applicability to reactor-relevant devices. This paper describes non-linear extended magnetohydrodynamic (MHD) simulations that use an experimental equilibrium from an enhanced D-alpha (EDA) H-mode in ASDEX Upgrade. Linear ideal MHD analysis indicates that the operational point lies slightly inside of the stable region. The non-linear simulations with the visco-resistive extended MHD code, JOREK, sustain non-axisymmetric perturbations that are linearly most unstable with toroidal mode numbers of $n = \{6 \ldots 9\}$, but non-linearly higher and lower n become driven and the low-n become dominant. The poloidal mode velocity during the linear phase is found to correspond to the expected velocity for resistive ballooning modes. The perturbations that exist in the simulations have somewhat smaller poloidal wavenumbers ($k_\theta \sim 0.1$–0.5 cm^{-1}) than the experimental expectations for the quasi-coherent mode in EDA, and cause non-negligible transport in both the heat and particle channels. In the transition from linear to non-linear phase, the mode frequency chirps down from approximately 35 kHz to 13 kHz, which corresponds approximately to the lower end of frequencies that are typically observed in EDA H-modes in ASDEX Upgrade.

[a] See Hoelzl *et al* 2021 (https://doi.org/10.1088/1741-4326/abf99f) for the JOREK Team.
[b] See Stroth *et al* 2022 (https://doi.org/10.1088/1741-4326/ac207f) for the ASDEX Upgrade Team.
[c] See Labit *et al* 2019 (https://doi.org/10.1088/1741-4326/ab2211) for the EUROfusion MST1 Team.
[*] Author to whom any correspondence should be addressed.

Keywords: plasma physics, magnetic confinement, non-linear simulations, magnetohydrodynamics, edge localised modes

(Some figures may appear in colour only in the online journal)

1. Introduction

Tokamak operation in the so-called high confinement mode (H-mode) naturally exhibits the onset of repetitive edge localised modes (ELMs), which can expel 5%–15% of the thermal energy stored in the magnetically confined plasma [1, 2]. For present-day devices, the energy expelled by ELMs is not a cause for concern as it does not exceed the material limits of the plasma facing components. However, for future devices like ITER, which will confine much larger amounts of thermal energy, it is foreseen that large ELMs will not be tolerable [3, 4]. Techniques that mitigate or suppress ELMs are actively investigated, but it is presently not possible to determine operational spaces of applicability in future machines. The same problem exists for regimes of operation that are either completely devoid of large ELMs or show only small ELMs that may be tolerable by the plasma facing components. Such no- and small-ELM regimes host some transport mechanism that prevents the edge pressure gradient and current density to grow unconstrained (which constitutes the reason why ELMs become excited) and flushes unwanted impurities out of the confined plasma [5–7].

One specific example of no-ELM regimes is the enhanced D-alpha (EDA) H-mode, which was first observed in the high-field tokamak, Alcator C-mod, with ion-cyclotron heating after a fresh boronisation [8, 9]. The EDA in C-mod constantly exhibits a quasi-coherent mode (QCM) primarily localised in the low-field side with a radial width of ∼2–5 mm and frequencies of 50–150 kHz. The QCM which appears to be located in the steep gradient region of the pedestal (at the radial electric field minimum in [10], but further outside in [11] which uses mirror Langmuir probes and may perturb the QCM). The influence of the QCM is observed in fluctuations of the density, electrostatic potential, and poloidal magnetic field [11–13]. As such, the QCM is thought to be an instability with electromagnetic character that constantly regulates the pedestal below the conditions where type-I ELMs are excited by causing continuous particle transport.

In addition to C-mod, the EDA has also been observed recently in EAST (closely related to a small ELM regime) [14], in ASDEX Upgrade with electron-cyclotron heating (ECRH) [15], and with a mixture of ECRH and neutral beam injection (NBI), including argon seeding [16]), and also in DIII-D [17]. For the latter two machines, which have similar sizes and current/magnetic field and are larger than C-mod, the QCM frequency lies in the range $f_{\mathrm{QCM}} = 15$–40 kHz. In AUG, the poloidal wavenumbers range between $k_\theta = 0.5$–$0.7\ \mathrm{cm}^{-1}$ ($k_\theta \rho_s = 0.025$–0.075, where $\rho_s = \sqrt{T_e m_i}/(eB)$ is the hybrid ion gyro-radius), while in C-mod k_θ ranges between 0.8 and $2.0\ \mathrm{cm}^{-1}$ [18]. These differences can be expected due to the different machine sizes; the toroidal mode numbers in question correspond to $n \approx 10$–20. In all devices, the QCM moves in the electron diamagnetic direction in the lab frame[8] and its frequency starts at larger values (roughly double), chirps down and remains in the aforementioned ranges for several confinement times. In AUG, the QCM typically has a narrow full-width at half-maximum at low fuelling and becomes broader upon increasing the gas puff [7]. During a small ELM regime dubbed quasi-continuous exhaust regime (QCE) [19, 20], a QCM has also been observed in ASDEX Upgrade under certain conditions. In contrast to low-fuelled EDA H-modes in AUG, it is found that the QCM present during the QCE regime displays a broader peak in the frequency spectrogram [21]. Thermal helium beam analysis of these two regimes measure fluctuations in the close vicinity to the separatrix with $f \sim 30$ kHz and filaments in the SOL with 0.1–2 kHz [22]. Magnetohydrodynamic (MHD) analysis of EDA indicates that the operational points lie slightly inside of the stability boundary for peeling–ballooning modes (the instabilities responsible for ELMs) with medium/high toroidal mode numbers ($n = \{10 \ldots 30\}$) and has been hypothesised that the QCM possibly relates more closely to resistive ballooning modes [23–26] or to drift ballooning modes [12].

The theoretical framework that relates to the QCM in EDA has not been yet fully explained [10]. Approaches from modelling include BOUT simulations for Alcator C-mod which connect resistive ballooning modes to the QCM in terms of several distinct features (poloidal wavenumber, frequency, velocity) [24]. BOUT++ has also been applied to study the QCM in C-mod and found good agreement with experiments; such studies suggest that resistive ballooning modes and drift-Alfvèn waves are the dominant instabilities during the EDA. The gyrokinetic code, GENE, has been used to study an EDA in ASDEX Upgrade, which did not find clear indications of the QCM (possibly due to difficulties encountered in resolving flux surfaces too close to the separatrix) [27].

Based on the same experimental equilibrium on which the GENE simulations had been based, first non-linear extended MHD simulations with the JOREK code [28, 29] are presented here. Non-axisymmetric perturbations in the simulations become excited and during the non-linear phase cover the frequency range from $8 \ldots 18$ kHz. Poloidal wavenumbers in the range $k_\theta \sim \{0.1 \ldots 0.5\}\ \mathrm{cm}^{-1}$ ($k_\theta \rho_s \sim \{0.01 \ldots 0.05\}$) with predominant ballooning features are found, and their poloidal mode velocity is found to closely relate to resistive (peeling-)ballooning modes. The dominant modes are

[8] In Alcator C-mod, mode propagation with respect to the plasma frame of reference (i.e. $v_{\mathrm{E}\times\mathrm{B}}$) has been separately reported in the ion diamagnetic direction for ICRF-heated plasmas as measured with gas puff imaging [10] and in the electron diamagnetic direction for ohmically-heated plasmas as measured with mirror Langmuir probes [11].

identified as resistive peeling–ballooning modes and are located at the maximum of the temperature gradient. Filaments are observed with $f \sim 2.3$ kHz, and peak heat-loads to the outer divertor target caused by the non-axisymmetric perturbations range from 3.2–12 MW m^{-2}.

In this paper, non-linear extended MHD simulations with initial conditions chosen from an EDA discharge in ASDEX Upgrade are presented. A brief description of the experimental discharge and the set-up of the simulations are presented in section 2, which includes results from linear ideal MHD calculations for the experimental equilibrium; a more complete description of the discharge can be found in [16, 27]. Thereafter, in section 3 the linearly unstable modes in the visco-resistive JOREK simulations are described in terms of their structure, growth-rates, mode velocity and direction of propagation and, finally, the resulting non-linear coupling that excites the linearly stable modes. The dominant modes during the non-linear phase (when the non-axisymmetric perturbations interact with the background plasma), the changes caused onto the magnetic fields, and the nature of the fluctuations across the pedestal are detailed in section 4. Finally, section 5 summarises and discusses the results presented.

2. Experimental discharge and simulation set-up

The simulations presented here take their initial conditions from AUG discharge #36330 in the time range 6.115–6.190 s, which is an argon-seeded EDA H-mode first described in [16], and that has been simulated with GENE [27]. This section presents several details on the experimental discharge as well as newly analysed data from the magnetic pick-up coil signals in section 2.1, and the JOREK simulation set-up together with relevant details from the model are discussed in section 2.2.

2.1. AUG #36330—Ar seeded EDA H-mode

The discharge used to set-up the simulations presented in this paper featured an EDA H-mode whose net power through the separatrix was feedback-controlled via argon seeding to be kept within the no-ELM window [16]. The EDA H-mode was entered by ramping up the external heating power and exited by reducing it, with no intrinsic limit on the duration of the regime. A stationary period with constant power was used for the simulation set-up. The discharge choice was mainly determined by the availability of high-quality diagnostic data, especially charge exchange recombination spectroscopy (CXRS), which is limited in most EDA H-modes of AUG. Detailed accounts of this experimental discharge can be found in [16, 27]; here is only a brief summary of the characteristics relevant for the present modelling work.

The discharge features a lower single null plasma with elongation $\kappa = 1.6$ and high triangularity ($\delta_{\text{lower}} = 0.49$ and $\delta_{\text{upper}} = 0.31$, $\delta_{\text{avg}} = 0.40$) operating in favourable ∇B drift direction (where the ion $\boldsymbol{B} \times \nabla B$ drift points towards the active X-point). The toroidal magnetic field is -2.5 T, the plasma current 0.8 MA ($-/+$ signs reflect toroidal direction running clockwise/counter-clockwise as seen from above), and the edge safety factor $q_{\psi_{\text{norm}}=0.95} = 4.86$. Figure 1 shows the traces of several quantities including the line-averaged density for lines-of-sight that probe the core and the edge (a), the divertor currents (b) where it can be seen that ELMs are not present, a frequency spectrogram from a helium beam signal (c) with a QCM with fluctuation frequency of $\sim\{20 \ldots 40\}$ kHz, and the heating mix (d). The latter is comprised of ECRH and NBI with 2.5 MW each from 5.9 to 6.3 s. The JOREK simulations are initialised from a time point within this phase.

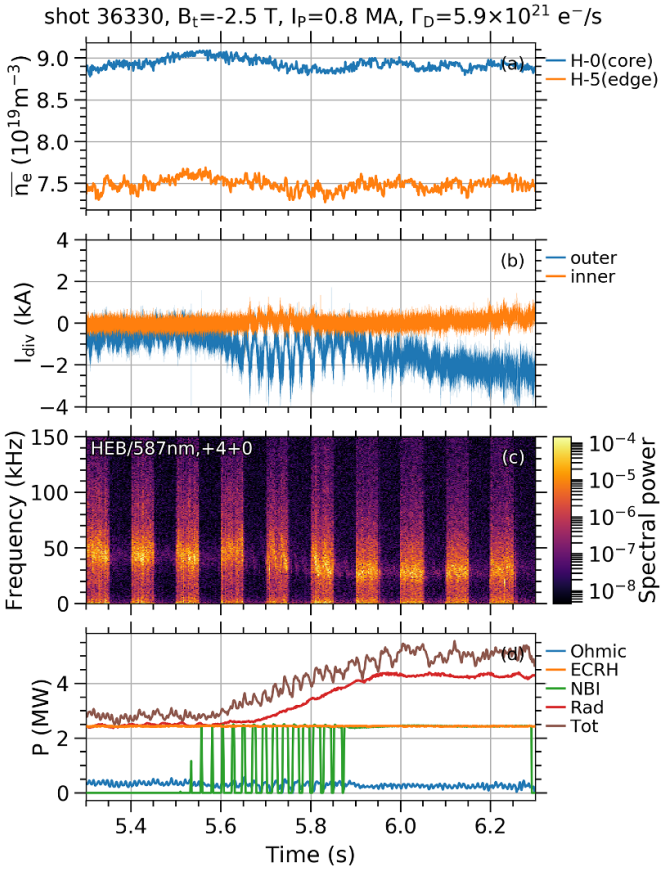

Figure 1. Traces of the AUG#36330 discharge for the time frame 5.3–6.3 s. (a) shows the core and edge line-integrated density measurements from interferometry, (b) the inner and outer divertor currents. The frequency spectrogram from a helium beam signal displays a dominant frequency around $f_{\text{QCM}} \approx 30$ kHz in (c); there are phases without signal because the helium valve is turned on and off periodically in order to subtract the background emission. And the heating power mixture together with the radiated power is shown in (d).

The absence of ELMs observed in figure 1(b) is likely attributed to the electromagnetic QCM with $f_{\text{QCM}} \approx 30$ kHz (ranges between 20 and 40 kHz), which can be observed in figure 1(c). The cross-field transport, including that caused by the QCM, causes a peak heat-flux onto the divertor targets of 5–10 MW m^{-2} (derived from Langmuir probes) [16].

The high-resolution equilibrium reconstruction with bootstrap constraint (the analytical Sauter formula [30, 31] is used) is generated with CLISTE [32] from data in the time

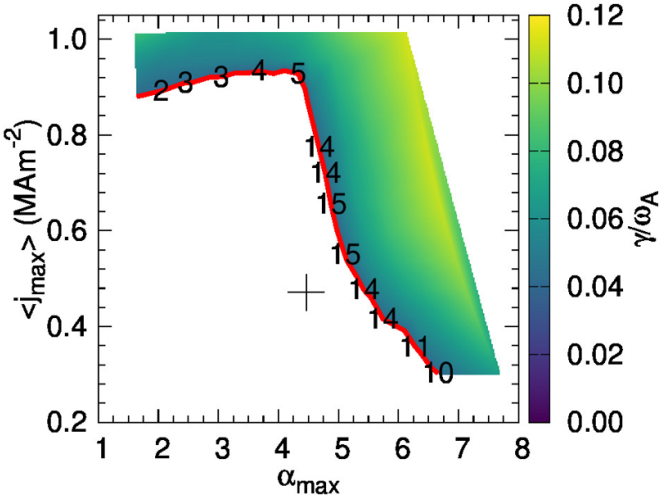

Figure 2. MISHKA-1 ideal linear MHD analysis of the equilibrium reconstruction at 6.165 s. The operational point at 6.165 s is found to be just inside of the ideal ballooning ($n \approx 15$) boundary. Beyond the stability boundary (red line), colour indicates the growth rate of the fastest growing mode normalised to the Alfvén frequency.

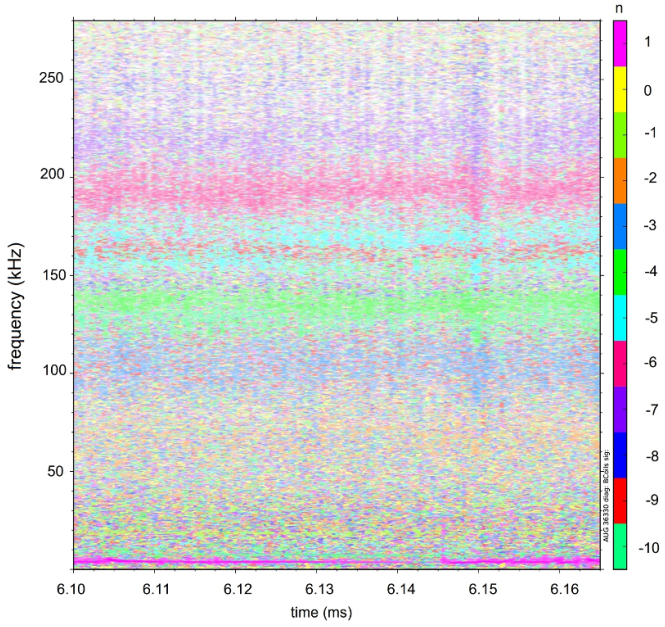

Figure 3. Cross phaseogram of several signals from magnetic pick-up coils in the equatorial midplane at different toroidal angles. Different colours indicate distinct toroidal mode numbers. In particular, $n = 3 \ldots 7$ are observed to be the relevant toroidal harmonics.

range 6.115 to 6.190 s, and it is used to initialise the JOREK simulations that will be discussed in depth in the following sections. Linear ideal MHD stability analysis with MISHKA-1 [33] is performed for this equilibrium, and shown in figure 2. The linear stability analysis finds the operational point to be slightly inside of the ($n \approx 15$) ballooning boundary. However, the MISHKA-1 simulations do not consider the separatrix, which has an important effect onto the stability of pedestal modes [29], and they neglect all non-ideal effects, notably the destabilizing resistivity and the stabilizing E × B and diamagnetic flows. Non-linear [34, 35] and linear [36] resistive MHD simulations have shown to move the ballooning boundary to lower pressure gradients, such that the operational point from figure 2 could easily be unstable to resistive (peeling-)ballooning modes. The movement of the ballooning boundary towards lower α seems to be independent of including diamagnetic effects; in the linear simulations of [36] diamagnetic effects were not included, but in the non-linear simulations the diamagnetic drift was considered and both observe the movement of the ballooning boundary. Indeed, the JOREK simulations that will be presented in the following sections find that the equilibrium is in fact unstable to resistive peeling–ballooning modes at realistic plasma resistivity, i.e. the ballooning stability boundary is shifted to lower α.

In addition to the QCM fluctuations that are observed in the helium beam diagnostic (which can also be observed in spectrograms of reflectometry, interferometry, electron cyclotron emission, magnetic pick-up coils closest to the plasma [15]), magnetic fluctuations are measured during the EDA H-mode phase. By considering several magnetic pick-up coils in the equatorial midplane, but at different toroidal angles, it is possible to identify the relevant toroidal mode numbers of $n = \{3 \ldots 7\}$. The cross-phaseogram that allows such analysis is shown in figure 3, but the precise nature of these modes, and their relation (if any) to the QCM is unclear as of yet. However, it is clear that these narrow-band fluctuations observed in the magnetic pick-up coils are a consistent feature of low-fuelled EDA H-mode discharges in AUG; these start to fade away upon including large amounts of gas puff. Coherent magnetic fluctuations were also observed in Alcator C-mod and reported in [37]. For AUG discharge #36330, the frequencies of the bands with distinct toroidal mode numbers can be written as $f_n = n \times 32.9\,\text{kHz}$, which is very close to the QCM frequency. However, the fact that f_{QCM} is so close to the base frequency of the magnetic fluctuations should not be interpreted as a direct relationship between the QCM and the magnetic fluctuations. In fact, depending on the discharge, the difference between the base frequency (f_n) with the QCM frequency can be as high as 15 kHz.

2.2. JOREK simulation set-up

As mentioned before, the JOREK simulations are initialised from an experimental reconstruction corresponding to 6.165 s in AUG discharge #36330. The corresponding simulations are carried out with the single-temperature reduced MHD model within JOREK and considers a perfectly conducting wall as boundary condition. Note that reduced MHD can be applied here allowing to reduce computational costs, since excellent agreement of reduced and full MHD models for pedestal applications has been shown [38]. For all simulations, the diamagnetic drift and bootstrap current source extensions are considered. The latter means that when profiles change non-linearly, the bootstrap current fraction changes according to

the Sauter analytical model [30, 31]; if profiles remain stationary, the bootstrap current fraction remains stationary as well. The change in bootstrap current source can only cause modifications to the current density profile if the non-linear profiles deviate from the initial profiles consistently for longer than the resistive current diffusion time scales. Using the diamagnetic drift means that the radial electric field well, which is characteristic of experimental E_r profiles in H-mode and proportional to $\nabla p_i/n_i$, is present in the simulations as has been shown in previous work [39]. A detailed account of the JOREK code, and of the single temperature reduced MHD model can be found in [28].

The input profiles of the density (n_e), temperature (T_e), radial electric field (E_r), and toroidal current density (j_φ) at the outboard midplane (flux-surface average for j_φ) are shown in figure 4 in black lines together with the experimental data points from Thompson scattering for T_e and n_e and from CXRS for T_i and E_r. Black crosses represent profiles after 10 ms of axisymmetric evolution (i.e. in the absence of perturbations). The E_r profile in green (which only spans until 1.00) comes from CXRS measurements of the impurity toroidal and poloidal velocity, temperature, and the force balance equation $E_r = \nabla p_\alpha/(eZ_\alpha n_\alpha) - \boldsymbol{v}_\alpha \times \boldsymbol{B}$, where α is the N^{7+} impurity species. The uncertainty of the E_r minimum is roughly $\sim\pm 4\,\mathrm{kV\,m^{-1}}$ [27].

It is evident that the axisymmetric profile does not match exactly with the measured profile, which is partly because the present simulations do not include a source for the toroidal rotation ($S_{v_\parallel}$) caused by the NBI torque and partly because the single temperature treatment cannot account for lower ion pressure gradients than electron and drives E_r to be more negative in the pedestal middle. This discrepancy between the E_r profiles would result in an effect on the pedestal instabilities since both the depth of the E_r well and the E × B shear play a role on the stability of peeling–ballooning modes. Nevertheless, studying the influence of $S_{v_\parallel}$ and/or of a two-temperature treatment on the stability and non-linear dynamics of pedestal instabilities requires dedicated studies and goes beyond the scope of the present work. Simulations with the two-temperature model available in JOREK [40], an appropriate choice for $S_{v_\parallel}$, and more advanced SOL modelling are foreseen for future work in order to properly assess the influence of such differences on the E_r profile. It is worth mentioning that as the non-axisymmetric simulation ($n = 0 \ldots 13$) develops (dashed purple line), the minimum value of E_r becomes shallower than the experimental measurements due to modifications to the profiles caused by the perturbations which will be described in detail in section 4.

The axisymmetric evolution of the profiles is determined by profiles of perpendicular diffusion coefficients and sources of particles and heat ($D_\perp$, $\chi_\perp$ and S_ρ, S_T respectively), which were designed to maintain the initial temperature, density, and current density profiles constant, as depicted by the fact that the full black lines and the black crosses in figure 4 overlap. The physical meaning of the diffusion coefficients corresponds to neoclassical and turbulent transport that cannot be simulated with JOREK, but is included with these ad-hoc

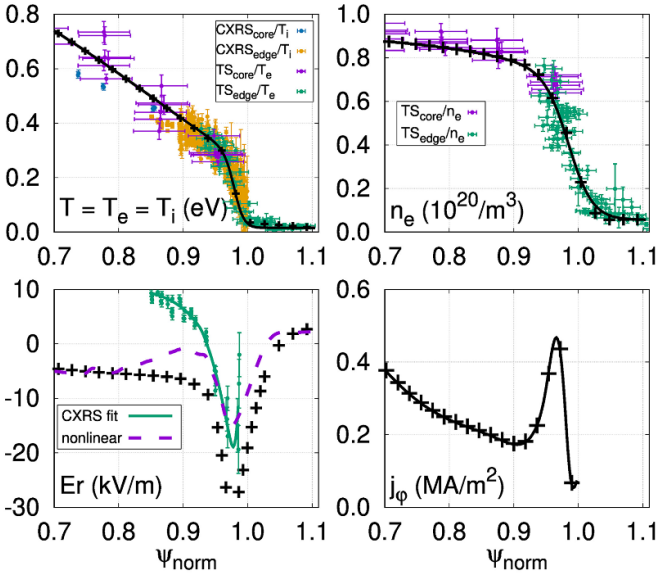

Figure 4. Experimental data points and input profiles of T_e, n_e, E_r, and j_φ. The latter has ohmic and bootstrap contributions and it is a flux-surface averaged profile, while the rest are profiles at the outboard midplane. Thompson scattering core and edge measurements are shown for T_e and n_e in purple and green, respectively. And charge exchange recombination spectroscopy data points for T_i. Black lines are the initial profiles and black crosses represent profiles after 10 ms of axisymmetric evolution. The experimental E_r is shown in green line, and a time-averaged midplane profile from the non-linear simulation of section 4 in dashed purple line. The discrepancy on the E_r profile between experiment and simulation is mostly due to the absence of $v_\parallel$ source and the assumption of $T_i = T_e$.

profiles. The diffusion coefficients and sources are determined with 1D profiles defined with the normalised poloidal flux, ψ_{norm}. In the location corresponding to the pedestal, the perpendicular diffusion coefficients feature an edge transport barrier, where $D_\perp$ and $\chi_\perp$ have very small values to represent the reduction of turbulent transport which characterises the H-mode pedestal. Once non-axisymmetric perturbations are included in the simulation, these can grow in amplitude and cause particle and heat transport, which will exist in addition to the cross-field transport from the ad-hoc diffusion profiles.

The parallel heat diffusion considers the Spitzer–Härm model, i.e. with a temperature dependency of $T^{5/2}$, which results in a parallel-to-perpendicular heat diffusion anisotropy on the order of $\chi_\parallel/\chi_\perp \sim 10^8$ (more details regarding the parallel heat diffusion in JOREK can be found in [28]). In terms of the resistivity, the Spitzer temperature dependency is considered, $T^{-3/2}$. The central value of resistivity is chosen such that the pedestal resistivity in the simulations ($\eta_{\mathrm{JOREK},95} \approx 1.0 \times 10^{-6}\,\Omega\mathrm{m}$) corresponds well to the experimentally-relevant value, i.e. the Spitzer resistivity with neoclassical and Z_{eff} corrections: $\eta_{\mathrm{exp},95} = 0.8 \times 10^{-6} \pm 0.4 \times 10^{-6}\,\Omega\mathrm{m}$. For the perpendicular viscosity, the profile follows the same temperature dependency as the resistivity, and the value on-axis is chosen such that the magnetic Prandtl number is around unity everywhere. The

parallel viscosity is a factor of 10 larger than the perpendicular viscosity. Further details regarding the viscous stress-tensor in JOREK can be found in [28].

The grid resolution required to resolve the simulations comprises 214 in the radial direction (i.e. from the axis to the perfectly conducting wall) which are accumulated primarily in the pedestal region such that the radial extent of one grid element is 1.28 mm, 354 in the poloidal direction, and 64 toroidal planes, which are needed to include 14 toroidal Fourier harmonics in the simulation: $n = 0 \ldots 13$. The temporal resolution in JOREK is not constrained by the CFL criterion since an implicit time stepping scheme is used; the time step used for the simulations corresponds to $\sqrt{\mu_0 \rho_0} = 0.6687\,\mu$s (except in the non-linear phase when it is sometimes necessary to decrease it by half to improve convergence of the iterative solver). Since the MHD model is valid for perturbations of low frequency (relative to the ion cyclotron frequency, $\Omega_i = eB/m \sim 10^8$ 1/s), perturbations that are faster cannot be adequately resolved with JOREK even if the time step were set to $\delta t \lesssim 1/\Omega_i \sim 0.01\sqrt{\mu_0 \rho_0}$.

Having described the experimental discharge, the simulation set-up and initial conditions, the focus is turned to describing the results during the linear phase.

3. Linear growth phase and dependencies

The present section describes the simulation results during the linear growth phase including linear growth rates, and the dynamics of the non-axisymmetric perturbations during the early non-linear phase, where three-wave interactions allow linearly stable modes to become non-linearly excited. The location and velocity of the modes during the linear phase is further discussed and their relation to resistive ballooning modes is highlighted.

3.1. Linear growth rates and early non-linear coupling

After 1 ms of axisymmetric simulation (during this time the parallel and poloidal flows establish and saturate), non-axisymmetric perturbations with toroidal Fourier harmonics $n = 1 \ldots 13$ are initialised at noise-amplitude. Figure 5 shows the non-axisymmetric perturbation magnetic energies (top) and their growth rates during the linear and early non-linear phases (bottom). It can be distinguished that there are linearly unstable modes ($n = \{4 \ldots 11\}$) and linearly stable modes ($n = \{1 \ldots 3\}$, 12, and 13) that become non-linearly excited during the early non-linear phase through three-wave interactions. Namely, a mode n_3 is driven by n_1 and n_2 provided that $n_3 = n_1 \pm n_2$ and the resulting growth-rate corresponds to $\gamma_{n_3} = \gamma_{n_1} + \gamma_{n_2}$ [41]. In this case several pairs of modes can contribute to driving a linearly stable mode. For example, $n_1 = 6$ and $n_2 = 6$ drive $n_3 = 12$, which is also driven by $n_1 = 5$ and $n_2 = 7$ and any other combination that satisfy $n_3 = n_1 \pm n_2$. The resulting growth-rate of $n = 12$ is given by contributions from all pairs of modes that satisfy $n_1 \pm n_2 = 12$, but it is mostly determined by the dominant mode pair that drive it.

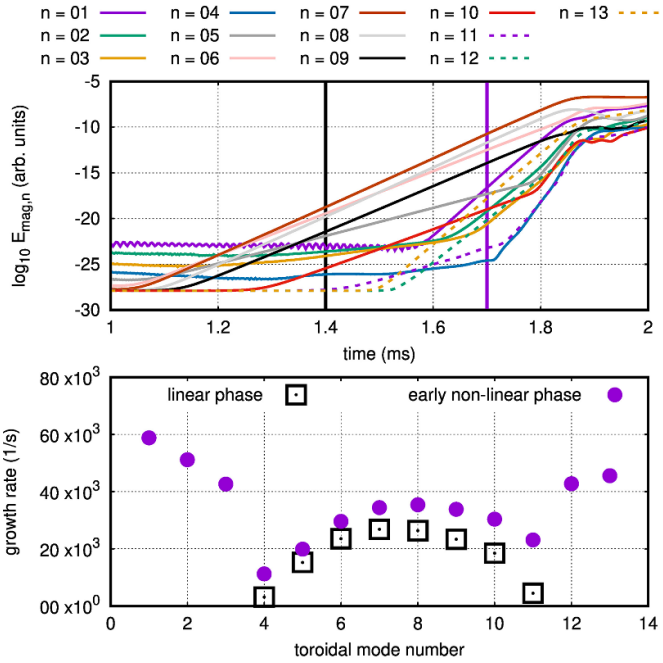

Figure 5. Top: magnetic energies of the non-axisymmetric perturbations during the linear phase ($\lesssim$1.5 ms) and early non-linear phase ($\gtrsim$1.5 ms). Bottom: growth-rates for the different toroidal mode numbers during the linear phase (black squares) and during the early non-linear phase (purple circles). Linearly stable modes become non-linearly destabilised due to three-wave interactions.

3.2. Mode location and velocity

The location of the linearly unstable modes is around $\psi_{\text{norm}} \approx 0.98$, which corresponds to the maximum temperature gradient and is consistent with experimental measurements from Alcator C-mod [10], and with recent observations from the EDA in ASDEX Upgrade with helium beam [21]. To clearly illustrate this, figure 6 (top) shows the derivatives of the electron temperature, pressure, and density with a black line, a dashed purple line, and a green line with marks, respectively. And figure 6 (bottom) shows the absolute value of the dominant complex m/n Fourier coefficients of the temperature perturbation normalised with the local temperature gradient in blue for $n = 6$, red for $n = 7$, black for $n = 8$, and orange for $n = 9$. With thicker lines, the resonant surface of $q = 6$ is shown for each harmonic with the respective colours. The dominant poloidal mode numbers during the linear phase are $m = \{35 \ldots 56\}$. The location of the mode maximum is shown with a vertical black line that spans both plots and corresponds to $\psi_{\text{norm}} = 0.983$, which sits almost exactly at the $\nabla_R(T_e)$ maximum.

Figure 7 shows the poloidal velocity of the perturbations along the flux-surface where the modes are located ($\psi_{\text{norm}} \approx 0.980$) during the linear phase ($t = 1.60$ ms) with green circles and during the non-linear phase ($t = 2.70$ ms) with black squares. Additionally, the plasma rotation velocity ($v_{\text{E}\times\text{B}} + \boldsymbol{v}_{\parallel} \cdot \boldsymbol{b}_\theta$) is also shown for either phase with a green dashed line and a black full line, respectively. The reduction in mode velocity between linear and non-linear

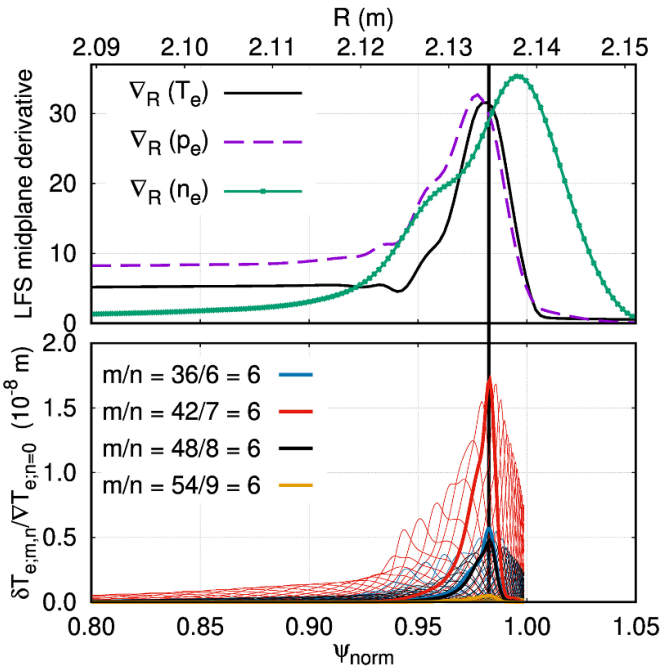

Figure 6. Top: derivatives (with respect to the major radius) at the outer midplane for T_e, p_e, and n_e profiles; the maximum gradient is located at $\psi_{\mathrm{norm}} = 0.980$, 0.977, and 0.995, respectively. Bottom: absolute value of various m/n Fourier coefficients for $\delta T_{e,m,n}/\nabla_R T_{e,n=0}$. The respective thick lines show the $m/n = 36/6$, $42/6$, $48/6$, and $54/9$ curves; namely at the $q = 6$ rational surface.

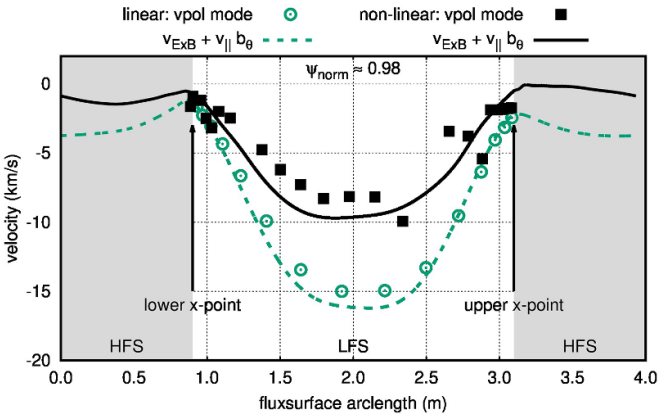

Figure 7. Poloidal velocity of the non-axisymmetric perturbations during the linear phase (at $t = 1.60$ ms) and non-linear phase ($t = 2.70$ ms) together with the poloidal velocity of the plasma along the $\psi_{\mathrm{norm}} \approx 0.98$ flux-surface.

phases will be discussed further in section 4. The movement of the non-axisymmetric perturbation is tracked along individual flux-surfaces and the distance travelled is used to obtain the poloidal mode velocity. From $\psi_{\mathrm{norm}} = 0.929$ until 0.987 (which is the outermost flux-surface with a reliable measurement of the velocity), the mode velocity at the outboard midplane is roughly $-15\,\mathrm{km\,s^{-1}}$, where the negative sign indicates movement in the electron diamagnetic drift direction. In the laboratory frame, the modes travel in the electron diamagnetic direction (negative velocities in figure 7) at all radial locations. In the plasma frame (i.e. the difference between the circles/squares and dashed/full line) the modes move in the ion diamagnetic direction at the outboard midplane with $v_{\mathrm{mode,pl.}} \approx 1\,\mathrm{km\,s^{-1}}$ only close to the location where the mode amplitude is maximised (from $\psi_{\mathrm{norm}} \approx 0.970$ until 0.982). Inward and outward of these locations, the modes move in the electron diamagnetic direction in the plasma frame. The mode velocity in the plasma frame is faster in radial locations further away from $\psi_{\mathrm{norm}} \approx 0.980$ since the modes experience rigid body rotation. For instance, $v_{\mathrm{mode,pl.}}(\psi_{\mathrm{norm}} = 0.934) = -9\,\mathrm{km\,s^{-1}}$, but $v_{\mathrm{mode,pl.}}(0.997) = -4.5\,\mathrm{km\,s^{-1}}$. Where the mode amplitude is maximised at 0.980, as mentioned before, it is approximately $+1\,\mathrm{km\,s^{-1}}$.

Experimental measurements from Alcator C-mod have measured the mode velocity in the laboratory frame to be in the electron diamagnetic direction always. In ohmic heated-only EDA H-modes, it has been reported that the QCM moves in the electron diamagnetic direction in the plasma frame (with measurements with mirror Langmuir probes) [11] and in ICRF-heated EDA in the ion diamagnetic direction in the plasma frame (with measurements from gas puff imaging) [10]. The latter showed that the mode amplitude is maximised at $\max(-\nabla T_e)$ and in that location $v_{\mathrm{mode,pl.}}$ is measured to be in the ion diamagnetic direction, but at larger velocities than observed in the simulations: in the range $\psi_{\mathrm{norm}} = \{0.95 \ldots 0.99\}$ the modes move with $\{+15 \ldots +7\}\,\mathrm{km\,s^{-1}}$ (in these experiments the poloidal projection of the parallel velocity is neglected; the mode velocity is compared with the E × B velocity). At this stage it is worth mentioning that the simplified scrape-off layer model used in the single-temperature JOREK simulation results in a radial electric field that is unrealistic in the SOL. Future work may then involve a more advanced SOL model [42] and a separation between ion and electron temperatures to understand the influence onto the mode dynamics, but this goes beyond the scope of the present work.

From a ballooning mode dispersion relation, the velocity of ideal ballooning modes has been reported in [43] to be $v_{\mathrm{E\times B}} + \boldsymbol{v}_{\parallel} \cdot \boldsymbol{b}_\theta + v^*_{i,\theta}/2$, where $v_{\mathrm{E\times B}}$ lies solely in the poloidal direction (this is one of the assumptions for the reduced MHD model in JOREK [39]), and for resistive ballooning modes to be $v_{\mathrm{E\times B}} + \boldsymbol{v}_{\parallel} \cdot \boldsymbol{b}_\theta$. The mode velocity extracted from the simulations is then compared to the local $v_\theta = \left(\boldsymbol{v}_{\mathrm{E\times B}} + \boldsymbol{v}_{\parallel}\right) \cdot \boldsymbol{b}_\theta$, which varies across and along flux-surfaces. The mode velocity is found to match best with the local v_θ where the mode amplitude is largest (i.e. $\psi_{\mathrm{norm}} \approx 0.980$), as mentioned before. This is an indication that the relevant modes are resistive peeling–ballooning modes.

The nature of the $n = 7$-dominated perturbation along a toroidal line at $(R, Z) = (2.130, 0.042)\,\mathrm{m}$, which is roughly at the maximum temperature gradient location ($\psi_{\mathrm{norm}} = 0.98$), is shown in figure 8. It shows variations of the density, temperature, and electrostatic potential during the linear phase (top) and during the non-linear phase (middle, and further explained in

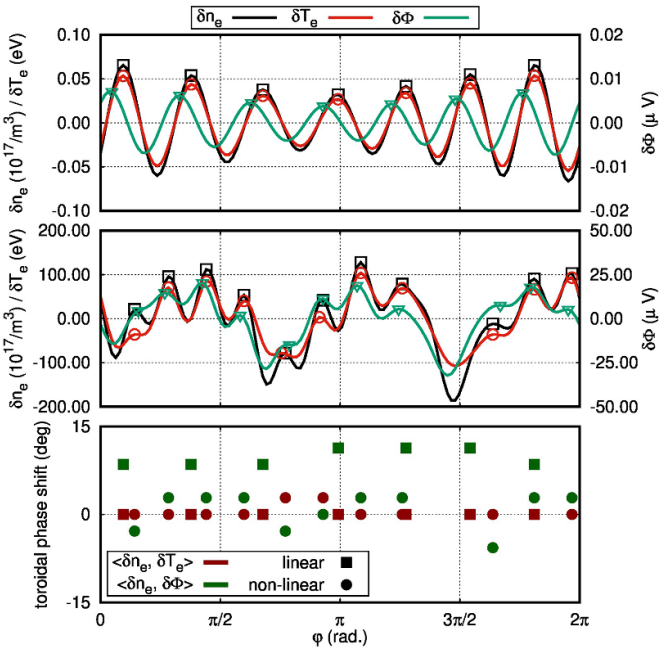

Figure 8. Perturbations of n_e, T_e, and Φ during the linear phase (top), during the non-linear phase (middle) along a toroidal line with constant $(R, Z_{\text{axis}}) = (2.130, 0.042)$ m. This location is at the outer midplane roughly where the temperature gradient is maximised. The cross-phases $\langle n_e, T_e \rangle$ in dark-red and $\langle n_e, \Phi \rangle$ in dark-green (bottom) are shown with squares for the linear phase and circles for the non-linear phase.

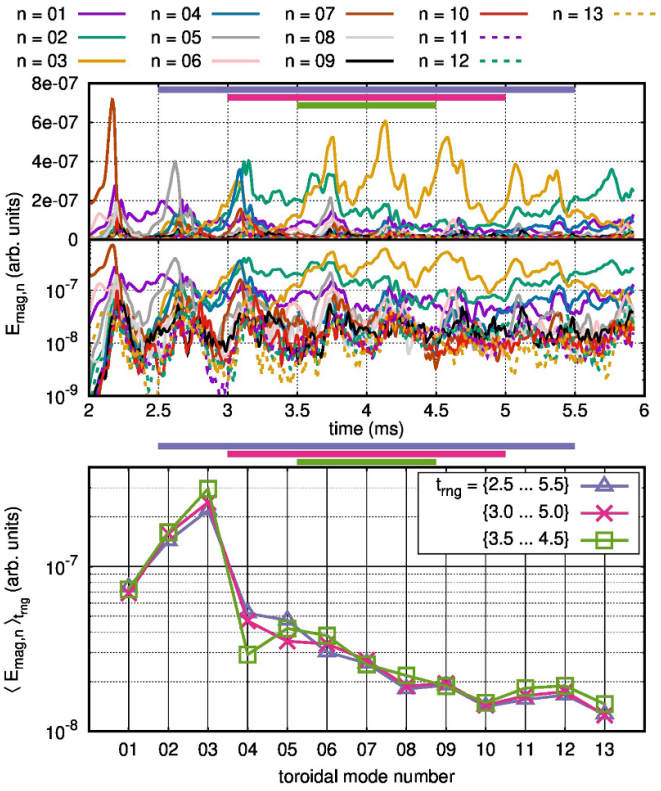

Figure 9. Linear (top) and logarithmic (middle) magnetic energies of the non-axisymmetric perturbations during the non-linear phase (from 2 to 6 ms). Bottom: three different temporally-averaged spectra centered around 4 ms with sample sizes of 1, 2, and 3 ms.

section 4). The cross-phase in the toroidal angle, φ, for $\langle n_e, T_e \rangle$ in dark-red and for $\langle n_e, \Phi \rangle$ in dark-green are shown for the linear phase with squares and for the non-linear phase with circles (bottom). During the linear phase, the perturbations of density and temperature are 'perfectly' in-phase with each-other, but have a cross-phase of $\sim 10^\circ$ with the electrostatic potential. In the following section, a detailed account of the non-linear phase is presented.

4. Non-linear simulation results

The previous section described the linear phase in terms of growth-rates, mode structure (dominant toroidal and poloidal mode numbers), location, and velocity. The present section details the temporal dynamics at play when the non-axisymmetric perturbations become large enough to interact with the axisymmetric background plasma. The non-linear phase observes a shift of dominant mode numbers from higher ($n = \{6 \ldots 9\}$) to lower ($n = \{2 \ldots 5\}$). The mode activity causes perturbations to the background magnetic field strong enough to create an ergodised layer in the pedestal (outward of $\psi_{\text{norm}} \approx 0.965$) and enhance parallel heat transport, which results in a depletion of the temperature pedestal. This stochastisation process takes place both due to resistive peeling–ballooning modes and to chains of magnetic islands at the edge and their non-linear interaction [44–47]. In addition, convective cells and filaments are formed and particle transport is generated which causes a depletion of the pedestal top density.

4.1. Shifting dominant toroidal mode numbers

The non-linear evolution of the non-axisymmetric perturbations (their magnetic energies) is shown in figure 9 from 2 to 6 ms in linear (top) and logarithmic (middle) scales, and three different temporally-averaged spectra (considering sample sizes of 1, 2, and 3 ms) centered around 4 ms (bottom). From the first two figures it is clear that the dominant mode numbers shift from higher-to-lower in time. There are two reasons for this effect 1) non-linear mode coupling gives energy from the higher-n perturbations that are linearly unstable ($n = \{4 \ldots 11\}$, but in particular $n = 6$, 7, and 8) to the lower-n that are linearly stable ($n = \{1 \ldots 3\}$) and 2) once the linearly most-unstable modes start to have an impact on the axisymmetric background they cause the pedestal density to become depleted, which in itself always has an effect on the linear spectrum. At this stage it is worth pointing out that during the non-linear phase neither the current density nor the temperature profiles experience significant variations in time (for the latter this can be seen in figure 10).

Figure 9 (bottom) clearly shows that once the non-linear phase is underway the dominant modes become $n = 2$ and 3. The $n = 3$-dominated structure can be distinguished in figure 8 (middle), where also several (11) local maxima can be observed. The presence of this $n = 11$ structure is a clear indication that high toroidal mode numbers are involved in the non-linear dynamics as well. During the non-linear phase,

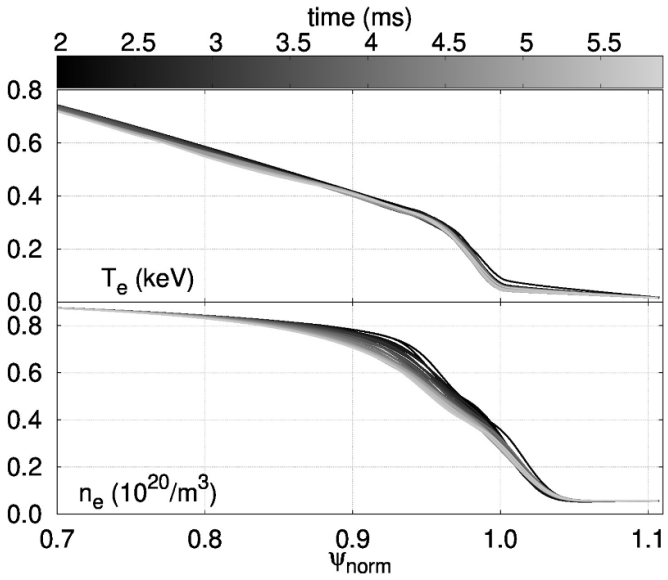

Figure 10. Toroidally-averaged edge temperature and density profiles at the outboard midplane during different times of the non-linear phase. The steady depletion of the pedestal due to the edge non-axisymmetric perturbations can be clearly observed (particularly in the density profiles).

density, temperature, and electrostatic potential are roughly in-phase (circles in the bottom part of figure 8). The effect of the non-axisymmetric perturbations onto the background plasma is detailed in the following.

4.2. Interaction with the background plasma

As the non-linear phase gets underway, the interaction between background plasma and non-axisymmetric perturbations causes heat and particle transport in a quasi-continuous manner; there are filaments formed in the simulations at a rate of ∼2.3 kHz which is comparable to observations from thermal helium beam [22]. The peak heat load to the divertor targets caused by the non-axisymmetric perturbations varies in time from 3.2 to 12.0 MW m^{-2} in the outer divertor, which is comparable to the experimental measurements from Langmuir probes (5–10 MW m^{-2}) [16]; for the inner divertor it is somewhat lower: 1.8–8.3 MW m^{-2}. This is in opposition to the transport caused by ELMs in JOREK simulations which, when studied at realistic resistivity and including diamagnetic effects and bootstrap current, feature transient transport due to individual ELMs with repetition frequencies around ∼120 Hz [46]. The rate of heat and particle losses resulting from the non-axisymmetric perturbations correspond to ∼2.5 MJ s^{-1} and ∼6.9×10^{21} ions s^{-1}, respectively. The evolution of edge density and temperature profiles (toroidally-averaged at the outboard midplane) during the non-linear phase is shown in figure 10. The steady depletion of the pedestal density, which may be partly responsible for the reduction in the dominant toroidal mode numbers during the non-linear phase, is clearly visible in the figure. The temperature profile also decreases, but it is less affected because the heating power remains constant and the number of particles in the pedestal is constantly decreasing.

4.3. Fluctuations across the pedestal

Locally, the temperature and density fluctuations in the pedestal are very large, of around $\delta T_e/\langle T_e\rangle \sim 50\%$ and $\delta n_e/\langle n_e\rangle \sim 40\%$, which is consistent with observations of the QCM for both C-mod [11] and AUG [15]. This, together with a spectrogram of the temperature fluctuations signal is shown in figure 11. In the spectrogram it is possible to determine that in the early non-linear phase (up to ∼2.2 ms) the fluctuations cover the frequency range $\{30\ldots45\}$ kHz and their frequency chirps down when the non-linear phase gets underway. This down-chirping is due to the fact that the radial electric field well becomes less deep due to the interaction between non-axisymmetric perturbations and background plasma. The frequency of the QCM in the experimental discharge can be observed in figure 1(*d*), and it is clear that the fluctuation present in the simulation during the linear phase corresponds well with the experimental f_{QCM}, albeit slightly larger in the simulations. It is worth reiterating at this stage that during the linear phase the E_r minimum in the simulations sits at $-29\,\mathrm{kV\,m^{-1}}$, while in the experiments it is calculated to be $-20 \pm 4\,\mathrm{kV\,m^{-1}}$. During the non-linear phase, the frequency remains relatively constant in a frequency range of $\{8\ldots18\}$ kHz.

The frequency of the fluctuations caused by non-axisymmetric modes does not experience variations with ψ_{norm} through the visible range ($\psi_{\mathrm{norm}} \approx 0.95$–$1.05$), therefore only a single radial location was chosen to present the spectrogram. On average, during the non-linear phase, the E_r minimum is $\sim -15\,\mathrm{kV\,m^{-1}}$, which is shallower than the experimental measurement, and therefore may be the reason why the fluctuation frequency in the non-linear phase of the simulation is lower than the experimental measurement. As a whole, these observations indicate that the resistive peeling–ballooning modes in the simulation could be related to the QCM.

The poloidal structure of the non-axisymmetric perturbations (along a single flux-surface) features a predominantly ballooning structure, i.e. localised on the low-field side with essentially no observable perturbations on the high-field side. In the outer midplane during the non-linear phase, the range of poloidal wavenumbers is $k_\theta \sim \{0.1\ldots0.5\}\ \mathrm{cm^{-1}}$ ($k_\theta \rho_s \sim \{0.01\ldots0.05\}$). For ASDEX Upgrade, based on measurements with helium beam, the range of poloidal wavenumers for the QCM is ∼0.5–0.7 cm^{-1} ($k_\theta \rho_s \sim \{0.025\ldots0.075\}$), and for fluctuations during the quasi-continuous exhaust regime, $k_\theta \sim \{0.4\ldots0.7\}\ \mathrm{cm^{-1}}$ [21]. As such, the poloidal wavenumbers present in the simulation hold a closer resemblance to the fluctuations measured during the QCE regime than the QCM during the EDA.

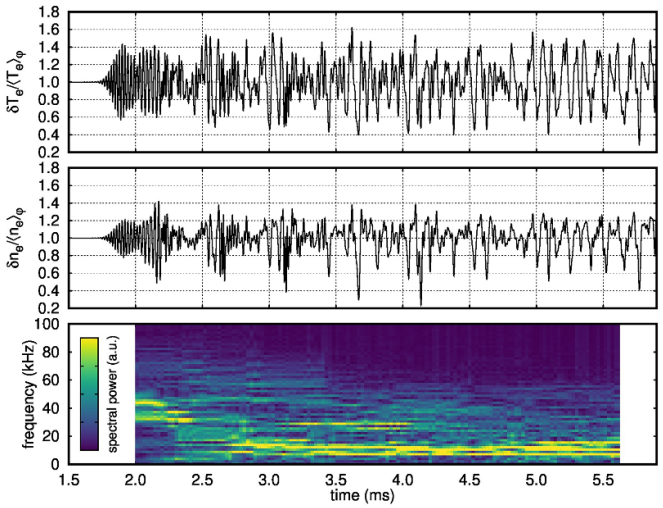

Figure 11. Temperature (top) and density (middle) fluctuations relative to the toroidally-averaged value in the location where the mode amplitude is maximised ($\psi_{\mathrm{norm}} \approx 0.98$). Bottom: spectrogram of the temperature fluctuations. At the end of the early non-linear phase ($t \lesssim 2.2$ ms) the pedestal fluctuations correspond to a frequency of roughly 35 kHz, but they chirp down to around 13 kHz in the non-linear phase.

5. Discussion and conclusions

In this paper, first non-linear extended MHD simulations that consider initial conditions from an experimental discharge in ASDEX Upgrade that corresponds to the EDA H-mode were presented, and the first JOREK simulations that probe the EDA H-mode altogether. The equilibrium reconstruction was carried out with the CLISTE code [32] and linear ideal MHD stability analysis with MISHKA-1 [33], which found the experimental point inside the stable region near the high-n ballooning boundary. The experimental discharge under consideration features the EDA with a QCM in a frequency range of 20–40 kHz and is completely devoid of large ELMs. The cross-field transport that prevents the pedestal from building up is thus thought to be caused by the QCM. In ASDEX Upgrade, magnetic pick-up coils in the outboard midplane observe fluctuations with toroidal mode numbers around $n = \{3 \ldots 7\}$ for the analysed discharge. The fundamental (i.e. $n = 1$) frequency of these fluctuations in the discharge under consideration is 32.9 kHz. The relationship between these magnetic fluctuations and the QCM is not yet clear; the fundamental frequency in some discharges matches that of the QCM, while in others it displays a difference to f_{QCM} by up to $\sim$15 kHz.

The simulations presented in this paper are carried out with the JOREK code [28, 29]. The linearly most unstable modes are found to be resistive peeling–ballooning modes with toroidal mode numbers in the range $n = \{6 \ldots 9\}$. These modes are identified to be resistive peeling–ballooning modes from their spatial structure (predominantly on the low-field side) and from their poloidal rotation velocity, which corresponds to that of resistive ballooning modes: $v_{\mathrm{E}\times\mathrm{B}} + v_{\parallel} \cdot \boldsymbol{b}_\theta$ [43]. The location of the maximum mode amplitude corresponds to the maximum of the electron temperature gradient, and at this location the poloidal mode velocity is in the ion diamagnetic direction in the plasma frame; both such observations are in qualitative agreement with experimental measurements from gas puff imaging in Alcator C-mod [10]. As the linearly most unstable modes (notably $n = 7$) grow in amplitude, they are able to non-linearly drive the linearly stable modes through three-wave interactions. As such, perturbations with lower and higher toroidal mode numbers (than $n = 4$ and 11, respectively) become excited. This early non-linear phase gives way to the fully non-linear phase when the non-axisymmetric perturbations grow large enough to interact with the background plasma. As the non-linear phase gets underway, the dominant toroidal mode number decreases from $n = 7$ to $n = 3$ but intermediate and high toroidal mode numbers remain relevant. In particular, a toroidal structure with $n = 11$ on top of the $n = 3$ structure is clearly observed in the $\max(-\nabla T_e)$ region. During this phase, particles and heat are quasi-continuously expelled through cross-field transport generated by the non-axisymmetric perturbations, and filaments with $f \sim 2.3$ kHz are observed in the SOL. The peak heat flux to the outer divertor caused by the non-axisymmetric perturbations ranges from 3.2 to 12.0 MW m^{-2}. Resulting from the cross-field transport induced by the perturbations, the pedestal density starts to become depleted while the temperature and current density are less visibly affected.

The density and temperature local fluctuations during the non-linear phase have large amplitudes, which is qualitatively consistent with measurements from EDA in ASDEX Upgrade [15]. Before the early non-linear phase comes to an end, these fluctuations lie on a frequency range of $\{30 \ldots 40\}$ kHz, which is consistent with the observations for the present discharge (before the density and temperature profiles are affected by the non-linear interaction between the non-axisymmetric perturbations and the background plasma). During the fully non-linear phase, when the density pedestal is depleting and the radial electric field well is becoming shallower, the fluctuation frequencies decrease to $\{8 \ldots 18\}$ kHz (which still sits at the lower end of the observed values of f_{QCM} in AUG [15]).

In summary, from the analysis performed of the JOREK simulations of an EDA H-mode, several quantitative and qualitative similarities are found with respect to experimental features and measurements of the QCM, filamentary dynamics, peak heat flux to the outer divertor target, and magnetic fluctuations captured by the pick-up coils. Further comparisons between non-linear extended MHD simulations and experimental measurements from the EDA H-mode are left for future work. In particular, a focus on more quantitative comparisons of the EDA H-mode itself and of its boundaries, including its relation to the QCE regime is foreseen. To this end, taking into account separate electron and ion temperatures, no-wall limit instead of the ideal wall boundary condition employed here, advanced SOL models, toroidal rotation sources, and potentially higher order finite Larmor radius corrections are under

consideration. Additional dependencies on the viscosity values, heat and particle sources, and impurity radiation can additionally be taken into account.

Acknowledgments

This work has been carried out within the framework of the EUROfusion Consortium, funded by the European Union via the Euratom Research and Training Programme (Grant Agreement No. 101052200 - EUROfusion). Views and opinions expressed are however those of the author(s) only and do not necessarily reflect those of the European Union or the European Commission. Neither the European Union nor the European Commission can be held responsible for them. In particular, A. Cathey received funding from a EUROfusion Researcher Grant and work package Tokamak Exploitation, and are acknowledged. The non-linear JOREK simulations were performed using the Marconi-Fusion supercomputer within the FUA36_MHD project.

ORCID iDs

A. Cathey https://orcid.org/0000-0001-7693-5556
M. Hoelzl https://orcid.org/0000-0001-7921-9176
L. Gil https://orcid.org/0000-0002-9970-2154
M.G. Dunne https://orcid.org/0000-0002-5259-9970
G.F. Harrer https://orcid.org/0000-0002-1150-3987

References

[1] Zohm H. 1996 Edge localized modes (ELMs) *Plasma Phys. Control. Fusion* **38** 105
[2] Leonard A.W. 2014 Edge-localized-modes in tokamaks *Phys. Plasmas* **21** 090501
[3] Eich T. *et al* 2017 ELM divertor peak energy fluence scaling to ITER with data from JET, MAST and ASDEX upgrade *Nucl. Mater. Energy* **12** 84–90
[4] Gunn J.P. *et al* 2017 Surface heat loads on the ITER divertor vertical targets *Nucl. Fusion* **57** 046025
[5] Oyama N. *et al* (The ITPA Pedestal Topical Group) 2006 Pedestal conditions for small ELM regimes in tokamaks *Plasma Phys. Control. Fusion* **48** A171–81
[6] Viezzer E. 2018 Access and sustainment of naturally ELM-free and small-ELM regimes *Nucl. Fusion* **58** 115002
[7] Viezzer E. *et al* 2023 Prospects of core-edge integrated no-ELM and small-ELM scenarios for future fusion devices *Nucl. Mater. Energy* **34** 101308
[8] Takase Y. *et al* 1997 Radiofrequency-heated enhanced confinement modes in the Alcator C-Mod tokamak *Phys. Plasmas* **4** 1647–53
[9] Greenwald M. *et al* 1999 Characterization of enhanced D-alpha high-confinement modes in Alcator C-Mod *Phys. Plasmas* **6** 1943–9
[10] Theiler C., Terry J.L., Edlund E., Cziegler I., Churchill R.M., Hughes J.W., LaBombard B. and Golfinopoulos T. (The Alcator C-Mod Team) 2017 Radial localization of edge modes in Alcator C-Mod pedestals using optical diagnostics *Plasma Phys. Control. Fusion* **59** 025016
[11] LaBombard B., Golfinopoulos T., Terry J.L., Brunner D., Davis E., Greenwald M. and Hughes J.W. 2014 New insights on boundary plasma turbulence and the quasi-coherent mode in Alcator C-Mod using a mirror Langmuir probe *Phys. Plasmas* **21** 056108
[12] Hubbard A.E. *et al* 2001 Pedestal profiles and fluctuations in C-Mod enhanced D-alpha H-modes *Phys. Plasmas* **8** 2033–40
[13] Snipes J.A., LaBombard B., Greenwald M., Hutchinson I.H., Irby J., Lin Y., Mazurenko A. and Porkolab M. 2001 The quasi-coherent signature of enhanced D-alpha H-mode in Alcator C-Mod *Plasma Phys. Control. Fusion* **43** L23
[14] Sun P.J. *et al* 2019 Experimental study of quasi-coherent mode using EAST tangential CO_2 laser collective scattering diagnostic in far-forward mode *Phys. Plasmas* **26** 012304
[15] Gil L. *et al* (The ASDEX Upgrade Team and The EUROfusion MST1 Team) 2020 Stationary ELM-free H-mode in ASDEX upgrade *Nucl. Fusion* **60** 054003
[16] Kallenbach A. *et al* (ASDEX Upgrade Team and EUROfusion MST1 team) 2020 Developments towards an ELM-free pedestal radiative cooling scenario using noble gas seeding in ASDEX upgrade *Nucl. Fusion* **61** 016002
[17] Paz-Soldan C. (The DIII-D Team) 2021 Plasma performance and operational space without ELMs in DIII-D *Plasma Phys. Control. Fusion* **63** 083001
[18] Terry J.L. *et al* 2005 Transport phenomena in the edge of Alcator C-Mod plasmas *Nucl. Fusion* **45** 1321
[19] Harrer G.F. *et al* 2018 Parameter dependences of small edge localized modes (ELMs) *Nucl. Fusion* **58** 112001
[20] Faitsch M., Eich T., Harrer G.F., Wolfrum E., Brida D., David P., Griener M. and Stroth U. 2021 Broadening of the power fall-off length in a high density, high confinement H-mode regime in ASDEX upgrade *Nucl. Mater. Energy* **26** 100890
[21] Kalis J. *et al* (The ASDEX Upgrade Team and The EUROfusion MST1 Team) 2023 Experimental characterization of the quasi-coherent mode in EDA H-mode and QCE scenarios at ASDEX upgrade *Nucl. Fusion* submitted
[22] Griener M. *et al* 2020 Continuous observation of filaments from the confined region to the far scrape-off layer *Nucl. Mater. Energy* **25** 100854
[23] Mossessian D.A., Snyder P.B., Greenwald M., Hughes J.W., Lin Y., Mazurenko A., Medvedev S., Wilson H.R. and Wolfe S. 2002 H-mode pedestal characteristics and mhd stability of the edge plasma in Alcator C-Mod *Plasma Phys. Control. Fusion* **44** 423
[24] Mazurenko A., Porkolab M., Mossessian D., Snipes J.A., Xu X.Q. and Nevins W.M. 2002 Experimental and theoretical study of quasicoherent fluctuations in enhanced D_α plasmas in the Alcator C-Mod tokamak *Phys. Rev. Lett.* **89** 225004
[25] Myra J.R. and D'Ippolito D.A. 2005 Edge instability regimes with applications to blob transport and the quasicoherent mode *Phys. Plasmas* **12** 092511
[26] Porkolab M., Rost J.C., Basse N., Dorris J., Edlund E., Lin L., Lin Y. and Wukitch S. 2006 Phase contrast imaging of waves and instabilities in high temperature magnetized fusion plasmas *IEEE Trans. Plasma Sci.* **34** 229–34
[27] Stimmel K. *et al* 2022 Gyrokinetic analysis of an argon-seeded EDA H-mode in ASDEX upgrade *J. Plasma Phys.* **88** 905880315
[28] Hoelzl M. *et al* 2021 The JOREK non-linear extended MHD code and applications to large-scale instabilities and their control in magnetically confined fusion plasmas *Nucl. Fusion* **61** 065001
[29] Huysmans G.T.A. and Czarny O. 2007 MHD stability in X-point geometry: simulation of ELMs *Nucl. Fusion* **47** 659
[30] Sauter O., Angioni C. and Lin-Liu Y.R. 1999 Neoclassical conductivity and bootstrap current formulas for general axisymmetric equilibria and arbitrary collisionality regime *Phys. Plasmas* **6** 2834–9

[31] Sauter O. and Angioni C. 2002 Erratum: "Neoclassical conductivity and bootstrap current formulas for general axisymmetric equilibria and arbitrary collisionality regime" [Phys. Plasmas 6, 2834 (1999)] *Phys. Plasmas* **9** 5140–2839
[32] McCarthy P.J. 1999 Analytical solutions to the Grad–Shafranov equation for tokamak equilibrium with dissimilar source functions *Phys. Plasmas* **6** 3554–60
[33] Mikhailovskii A.B., Huysmans G.T.A., Kerner W.O.K. and Sharapov S.E. 1997 Optimization of computational MHD normal-mode analysis for tokamaks *Plasma Phys. Rep.* **23** 844–57
[34] Cathey A., Hoelzl M., Harrer G., Dunne M.G., Huijsmans G.T.A., Lackner K., Pamela S.J.P., Wolfrum E. and Günter S. (The JOREK Team, The ASDEX Upgrade Team and The EUROfusion MST1 Team) 2022 MHD simulations of small ELMs at low triangularity in ASDEX upgrade *Plasma Phys. Control. Fusion* **64** 054011
[35] Kleiner A., Ferraro N.M., Diallo A. and Canal G.P. 2021 Importance of resistivity on edge-localized mode onset in spherical tokamaks *Nucl. Fusion* **61** 064002
[36] Nyström H., Frassinetti L., Saarelma S., Huijsmans G.T.A., Perez von Thun C., Maggi C.F. and Hillesheim J.C. (JET Contributors) 2022 Effect of resistivity on the pedestal MHD stability in JET *Nucl. Fusion* **62** 126045
[37] Snipes J.A. *et al* 1998 ELMs and fast edge fluctuations in Alcator C-Mod *Plasma Phys. Control. Fusion* **40** 765
[38] Pamela S.J.P., Bhole A., Huijsmans G.T.A., Nkonga B., Hoelzl M., Krebs I. and Strumberger E. 2020 Extended full-MHD simulation of non-linear instabilities in tokamak plasmas *Phys. Plasmas* **27** 102510
[39] Cathey A., Hoelzl M., Futatani S., Lang P.T., Lackner K., Huijsmans G.T.A., Pamela S.J.P. and Günter S. (The JOREK Team, The ASDEX Upgrade Team and The EUROfusion MST1 Team) 2021 Comparing spontaneous and pellet-triggered ELMs via non-linear extended mhd simulations *Plasma Phys. Control. Fusion* **63** 075016
[40] Smith S.F., Pamela S.J.P., Fil A., Hölzl M., Huijsmans G.T.A., Kirk A., Moulton D., Myatra O., Thornton A.J. and Wilson H.R. (The JOREK Team) 2020 Simulations of edge localised mode instabilities in MAST-U Super-X tokamak plasmas *Nucl. Fusion* **60** 066021
[41] Krebs I., Hoelzl M., Lackner K. and Günter S. 2013 Nonlinear excitation of low-n harmonics in reduced magnetohydrodynamic simulations of edge-localized modes *Phys. Plasmas* **20** 082506
[42] Korving S.Q., Huijsmans G.T.A., Park J.-S. and Loarte A. (The JOREK Team) 2023 Development of the neutral model in the nonlinear MHD code JOREK: application to E × B drifts in ITER PFPO-1 plasmas *Phys. Plasmas* **30** accepted
[43] Morales J.A. *et al* 2016 Edge localized mode rotation and the nonlinear dynamics of filaments *Phys. Plasmas* **23** 042513
[44] Huysmans G.T.A., Pamela S., van der Plas E. and Ramet P. 2009 Non-linear MHD simulations of edge localized modes (ELMs) *Plasma Phys. Control. Fusion* **51** 124012
[45] Pamela S.J.P., Huijsmans G.T.A., Kirk A., Chapman I.T., Harrison J.R., Scannell R., Thornton A.J., Becoulet M. and Orain F. (The MAST Team) 2013 Resistive MHD simulation of edge-localized-modes for double-null discharges in the MAST device *Plasma Phys. Control. Fusion* **55** 095001
[46] Cathey A., Hoelzl M., Lackner K., Huijsmans G.T.A., Dunne M.G., Wolfrum E., Pamela S.J.P., Orain F. and Günter S. (The JOREK Team, The ASDEX Upgrade Team and The EUROfusion MST1 Team) 2020 Non-linear extended MHD simulations of type-I edge localised mode cycles in ASDEX Upgrade and their underlying triggering mechanism *Nucl. Fusion* **60** 124007
[47] Rhee T., Kim S.S., Jhang H., Park G.Y. and Singh R. 2015 A mechanism for magnetic field stochastization and energy release during an edge pedestal collapse *Nucl. Fusion* **55** 032004